Karl Iagnemma
Steven Dubowsky

Massachusetts Institute of Technology
Department of Mechanical Engineering
Cambridge, MA 02139, USA
kdi@mit.edu

Traction Control of Wheeled Robotic Vehicles in Rough Terrain with Application to Planetary Rovers

Abstract

Mobile robots are being developed for high-risk missions in rough terrain situations, such as planetary exploration. Here, a rough-terrain control methodology is presented that exploits the actuator redundancy found in multiwheeled mobile robot systems to improve ground traction and reduce power consumption. The algorithm optimizes individual wheel torque based on multiple optimization criteria, which are a function of the local terrain profile. A key element of the method is to be able to include estimates of wheel–terrain contact angles and soil characteristics. A method using an extended Kalman filter is presented for estimating these angles using simple on-board sensors. Simulation and experimental results for a micro-rover traversing challenging terrain demonstrate the effectiveness of the algorithm.

KEY WORDS—control, mobile robots, planetary rovers, rough terrain, wheel-terrain interaction

1. Introduction and Background

Mobile robots are being developed for high-risk missions in rough terrain environments. One successful example has been the NASA Jet Propulsion Laboratory (JPL) Sojourner Mars rover (Golombek 1998). Future planetary missions will require mobile robots to perform difficult tasks in more challenging terrain than encountered by Sojourner (Schenker et al. 2003; Volpe, 2003). Other examples of rough terrain applications for robotic systems can be found in the forestry and mining industries, and in hazardous material handling applications (Osborn 1989; Cunningham et al. 1998; Gonthier and Papadopolous 1998).

The International Journal of Robotics Research
Vol. 23, No. 10–11, October–November 2004, pp. 1029-1040,
DOI: 10.1177/0278364904047392

In rough terrain, it is critical for mobile robots to maintain adequate wheel traction. Excessive wheel slip could cause a rover to lose mobility and become trapped. Substantial work has been performed on traction control of passenger vehicles on flat surfaces (Tan and Chin 1992; Lee and Tomizuka 1996; Kawabe et al. 1997). This work is not applicable to low-speed, rough terrain rovers because in these vehicles wheel slip is caused primarily by kinematic incompatibility or loose soil conditions, rather than "breakaway" wheel acceleration. Traction control for low-speed mobile robots on flat surfaces has been studied (Reister and Unseren 1993). Later work has considered the important effects of terrain unevenness on traction control (Sreenivasan and Waldron 1996). This work assumes a priori knowledge of terrain geometry and soil characteristics. However, in applications such as planetary exploration this information is usually unknown. A fuzzy-logic traction control algorithm for a rocker-bogie rover that did not assume knowledge of terrain geometry has been developed (Hacot 1998). This approach is based on heuristic rules related to vehicle mechanics.

Knowledge of terrain information is critical to the traction control problem. A key variable for traction algorithms is the contact angles between the vehicle wheels and the terrain (Sreenivasan and Wilcox 1994; Farritor, Hacot, and Dubowsky 1998). Physical measurement of this angle is difficult. Researchers have proposed installing multi-axis force sensors at each wheel to measure the contact force direction, and inferring the ground-contact angle from the force data (Sreenivasan and Wilcox 1994). However, wheel-hub mounted multi-axis force sensors would be costly and complex. Complexity reduces reliability and adds weight, two factors that carry severe penalties for planetary exploration applications. Other researchers have proposed using vehicle models and terrain map data to estimate wheel–terrain

contact angles (Balaram 2000). However, accurate terrain map data are difficult to obtain. Additionally, terrain may deform during robot traversal, causing estimation error.

Knowledge of terrain parameters is another important input to traction control algorithms. For rigid terrain, a force coefficient is often assumed or estimated. In deformable terrain, parameters such as cohesion and internal friction angle can be used to estimate terrain shear strength (Wong 2001). Researchers have developed methods for estimating these parameters on-line (Iagnemma, Shibly, and Dubowsky 2002; Iagnemma et al. 2003).

In this paper we present a control methodology for vehicles with redundant drive wheels for improved traction or reduced power consumption. In highly uneven terrain, traction is optimized. In benign terrain, power consumption is minimized. A method is presented for estimating wheel–terrain contact angles of mobile robots using simple on-board sensors. The algorithm is based on rigid-body kinematic equations and uses sensors such as vehicle inclinometers and wheel tachometers. It does not require the use of force sensors. The method uses an extended Kalman filter to fuse noisy sensor signals. A terrain parameter estimation technique is also briefly discussed.

Simulation results are presented for a planar model of a four-wheeled rover on uneven terrain. It is shown that the rough-terrain control method leads to increased traction and improved power consumption as compared to traditional individual-wheel velocity control. It is also shown that the wheel–terrain contact angle estimation method can accurately estimate contact angles in the presence of sensor noise and wheel slip. Experimental results for a six-wheeled microrover traversing a ditch show that the proposed control method increases the net forward wheel thrust, and improves rover mobility.

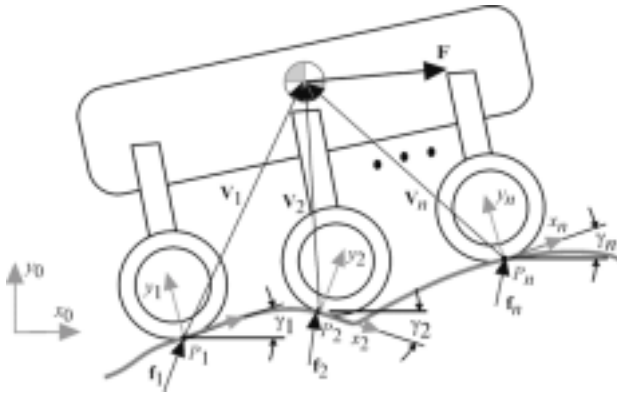

Fig. 1. The $n-$wheeled vehicle on uneven terrain.

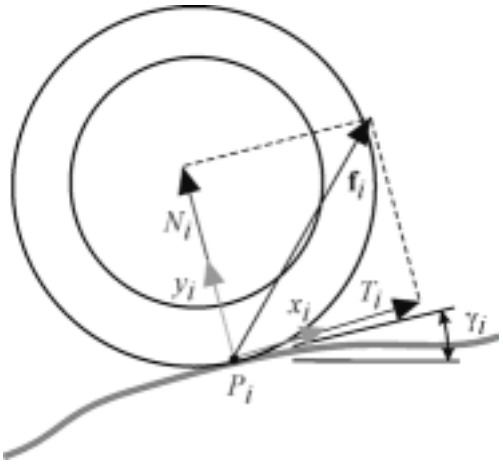

Fig. 2. Wheel–terrain interface on uneven terrain.

2. Rough-Terrain Control Problem Statement

Consider an n-wheeled vehicle on uneven terrain, as shown in Figure 1. The vehicle is assumed to be skid-steered, so only forces in the $x_o - y_o$ plane of the vehicle are considered. It is also assumed that each wheel makes contact with the terrain at a single point, denoted $P_i, i = \{1, \ldots, n\}$. This is a reasonable assumption for vehicles with rigid wheels (such as currently planned Mars rovers) moving on firm terrain. For vehicles moving on deformable terrain, distributed wheel–terrain contact stresses can be resolved to forces at a single point. Vectors from the points P_i to the vehicle center of mass are denoted $\mathbf{V}_i = [V_i^x V_i^y]^T, i = \{1, \ldots, n\}$ and are expressed in the corresponding local frame $\{xyz_i\}$ fixed at P_i. The 3×1 vector $\mathbf{F}$ is expressed in the inertial frame $\{xyz_o\}$ and represents the summed effects of vehicle gravitational forces, inertial forces, forces due to manipulation, and forces due to interaction with the environment or other robots.

A wheel–terrain contact force exists at each point P_i and is denoted $\mathbf{f}_i = [T_i N_i]^T$ (see Figure 2). The vector is expressed in the local frame $\{xyz_i\}$ and can be decomposed into a tractive force T_i tangent to the wheel–terrain contact plane and a normal force N_i normal to the wheel–terrain contact plane. It is assumed that there are no moments acting at the wheel–terrain interface. The angles $\gamma_i, i = \{1, \ldots, n\}$ represent the angle between the horizontal and the wheel–terrain contact plane.

For the planar system above, quasi-static force balance equations can be written as

$$\begin{bmatrix} {}^0\mathbf{R}_1 & {}^0\mathbf{R}_2 & \cdots & {}^0\mathbf{R}_n \\ V_1^y & -V_1^x\, V_2^y & -V_2^x \cdots V_n^y & -V_n^x \end{bmatrix} \begin{bmatrix} \mathbf{f}_1 \\ \vdots \\ \mathbf{f}_n \end{bmatrix} = \begin{bmatrix} F_x \\ F_y \\ M_z \end{bmatrix} \tag{1}$$

where ${}^i\mathbf{R}_j$ represents a 2×2 matrix transforming a vector expressed in frame j to one expressed in frame i.

Equation (1) represents the quasi-static force balance on the vehicle and is often referred to as the force distribution equation (Hung, Orin, and Waldron 1999). It neglects dynamic effects, which are small in low-speed planetary exploration vehicles. Force distribution has been studied for general kinematic chains and legged vehicles (Kumar and Waldron 1988, 1990). Efficient formulation of the force distribution equations for more general vehicles has been addressed (Hung, Orin, and Waldron 1999).

Equation (1) can be written in general matrix form as

$$\mathbf{G}\mathbf{x} = \mathbf{F} \tag{2}$$

where the matrix $\mathbf{G}$ is a function of the vehicle geometry, the wheel–terrain contact locations and the wheel–terrain contact angles, $\mathbf{x} = [T_1 N_1 \ldots T_n N_n]^T$, and $\mathbf{F} = [F_x F_y M_z]^T$. In the proposed control approach, $\mathbf{F}$ is an input vector. Note that $\mathbf{F}$ is directed along the body axis for normal forward driving. Wheel torques are thus sought that result in the desired force vector $\mathbf{F}$.

Equation (2) represents an underconstrained problem (ignoring the trivial case of a one-wheeled vehicle). There are an infinite number of wheel–terrain contact forces T_i and N_i that balance the vector $\mathbf{F}$. In general, a planar system with n wheel–terrain contact points possesses $(2n - 3)$ degrees of redundancy. The goal of rough terrain control is to find a set of wheel–terrain contact forces (which are modified by means of independently controlled motor torques) that satisfy the force distribution equations and the problem constraints while optimizing an aspect of system performance. The control problem can thus be framed as an optimization problem, and be generally stated as follows: optimize system performance subject to the equality constraint $\mathbf{G}\mathbf{x} = \mathbf{F}$ while satisfying all problem physical constraints.

A simple approach to solving underconstrained systems is via the pseudo-inverse or least-squares solution, defined as $\mathbf{x}^+ = \left(\mathbf{G}^T\mathbf{G}\right)^{-1}\mathbf{G}^T\mathbf{F}$, assuming $\mathbf{G}$ has full column rank. However, while this solution is computationally inexpensive, it does not guarantee satisfaction of the problem's physical constraints. The problem's physical constraints and an optimization framework for solving eq. (2) are discussed below.

The above analysis has considered a two-dimensional system. The effects of motion on general (i.e., three-dimensional) terrain can be considered by noting that $\mathbf{F}$ is influenced by the vehicle's body roll. Since roll can be easily sensed, the vertical component of $\mathbf{F}$ can be modified on-line. This changes the load balance (and thus the available tractive force) on each side of the vehicle. Note that body roll will also influence wheel–terrain longitudinal forces. These effects are not considered here.

3. Wheel–Terrain Contact Force Optimization

Planetary mobile robots must maintain good wheel traction in highly challenging terrain. However, during long-range traverses over benign terrain, it is important for rovers to exhibit good power efficiency. Optimization of wheel–terrain contact forces is therefore performed using two criteria: maximum traction or minimum power consumption. These criteria are discussed below.

3.1. Optimization Criteria

An optimization criterion for maximizing traction at the wheel–terrain interface is developed based on the observation that the maximum tractive force a terrain can bear increases with increasing normal force (Bekker 1969). Thus, to avoid terrain failure and resulting gross wheel slip, the control algorithm should seek to minimize the maximum ratio of the tractive force to the normal force. An objective function representing this ratio can be written as

$$R = \max_i \left\{ \frac{T_i}{N_i} \right\}. \tag{3}$$

A similar criterion has been developed in Sreenivasan and Wilcox (1994) and an analytical solution to the optimization problem has been developed for a two-wheeled vehicle. For the general problem, the optimal force distribution (eq. (1)) can be solved with standard optimization techniques (Chung and Waldron 1993).

An optimization criterion for minimum power consumption can be developed based on the fact that the power consumed by a DC motor-driven wheeled vehicle using PWM amplifiers can be estimated by the power dissipation in the motor resistances (Dubowsky, Moore, and Sunada 1995). Power consumption of the vehicle is related to the motor torques as

$$P = \frac{Rn^2}{K_t^2} \sum_{i=1}^{n} \Gamma_i^2 \tag{4}$$

where R is the motor resistance, K_t is the motor torque constant, n is the motor gear ratio, and Γ_i is the torque applied by the ith motor. The power consumption can then be related to the tractive force T_i by

$$P = \frac{Rn^2 r^2}{K_t^2} \sum_{i=1}^{n} T_i^2 \tag{5}$$

where r is the wheel radius.

Here we have assumed that on benign terrain with little wheel sinkage, the tractive force is the product of the applied wheel torque and the wheel radius. Thus, to minimize power consumption the control algorithm should seek to minimize P. In the case of large wheel sinkage and/or substantial wheel slip, the tractive force (i.e., the net wheel thrust) is a function of the wheel sinkage, slip, and various terrain parameters. However, in this case the tractive force still remains proportional to the wheel torque (Wong 2001).

Based on eqs. (3) and (5) a dual-criteria objective function can be developed, which optimizes for maximum traction or minimum power consumption depending on the terrain profile. In rough terrain, traction should be maximized. In benign terrain, power consumption should be minimized. Terrain roughness can be determined by examining the values of the wheel–terrain contact angles. Consider the switching function S

$$S = \begin{cases} 1 & if \max_i \{\ |\gamma_i|\ \} > C \\ 0 & otherwise \end{cases} \tag{6}$$

where C is an arbitrary threshold level. This function distinguishes between benign and challenging terrain by examining the steepest local terrain slope. Numerous other methods could be used to assess terrain difficulty. For example, a vehicle equipped with a three-dimensional vision system could characterize unevenness by considering local terrain elevation data.

A dual-criteria objective function which combines eqs. (3), (5), and (6) can then be expressed as

$$Q = RS + T(1 - S). \tag{7}$$

Thus, the vehicle force distribution will be optimized for either maximum traction or minimum power consumption, depending on the local terrain profile. The frequency at which Q is evaluated should be a function of the expected spatial frequency of the terrain in the robot's operating region.

3.2. Problem Constraints

Optimization of the force distribution problem must consider physical constraints of the system. One such constraint is that all rover wheels should remain in contact with the terrain. This can be expressed by ensuring that all wheel–terrain normal forces N_i remain positive, or

$$N_i > 0 \ \forall\, i, i = \{1 \ldots n\}. \tag{8}$$

The second constraint is that the wheel torques must remain within the saturation limits of the actuator, or

$$\Gamma_i^{min} \leqslant (T_i \cdot r) \leqslant \Gamma_i^{max} \ \forall\, i,\ i = \{1 \ldots n\}. \tag{9}$$

The third is that the tractive force exerted on the terrain must not exceed the maximum force that the terrain can bear. The simplest approximation of this constraint is a Coulomb friction or "force coefficient" model

$$T_i \leqslant \mu N_i \ \forall\, i, i = \{1 \ldots n\}, \tag{10}$$

where μ is the wheel–terrain force coefficient. This approximation is reasonable for rigid wheels traveling over rigid terrain. For rigid wheels in deformable terrain, the maximum shear strength of the terrain can be computed as (Bekker 1956)

$$\tau^{max} = c + \left(N_i / A_i\right) \tan(\phi) \tag{11}$$

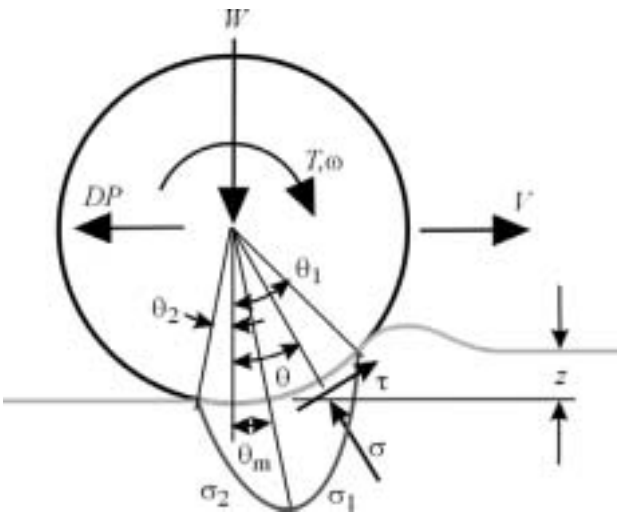

Fig. 3. Free-body diagram of rigid wheel on deformable terrain.

where c is the terrain cohesion, ϕ is the terrain internal friction angle, and A is an estimate of the wheel–terrain contact area. Thus, the terrain strength constraint can be written for deformable terrain as

$$\left(T_i / A_i\right) \leqslant \tau_i^{max} \ \forall\, i, i = \{1 \ldots n\}. \tag{12}$$

A priori estimates of c and ϕ an be used if the terrain properties are known in advance. If the parameters are unknown or variable, estimation techniques can be employed.

A method for on-line estimation of c and ϕ has been developed (Iagnemma, Shibley, and Dubowsky 2002). The algorithm relies on a simplified form of classical terramechanics equations, derived from quasi-static analysis of wheel–terrain interaction (see Figure 3). The method uses a linear least-squares estimator to compute c and ϕ in real time. This allows a rover to optimize its wheel traction to locally changing terrain conditions. In this paper, however, we assume a priori knowledge of c and ϕ for simplicity.

4. Wheel–Terrain Contact Angle Estimation

To solve the optimization problem discussed above, the local wheel–terrain contact angles must be known. Here, we present a method for estimating wheel–terrain contact angles from simple on-board rover sensors.

Consider a planar two-wheeled system on uneven terrain (see Figure 4). In this analysis the terrain is assumed to be rigid, and the wheels are assumed to make point contact with the terrain. For rigid wheels on deformable terrain, the single-point assumption no longer holds. However, an "effective" wheel–terrain contact angle is defined as the angular direction

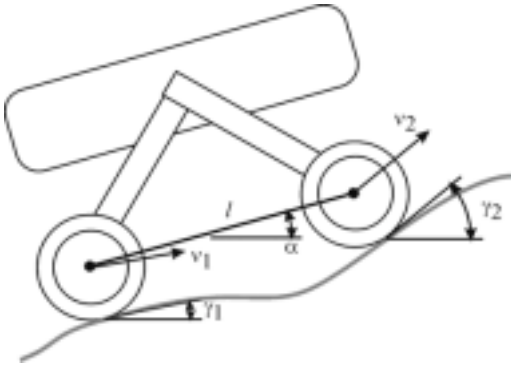

Fig. 4. Planar two-wheeled mobile robot.

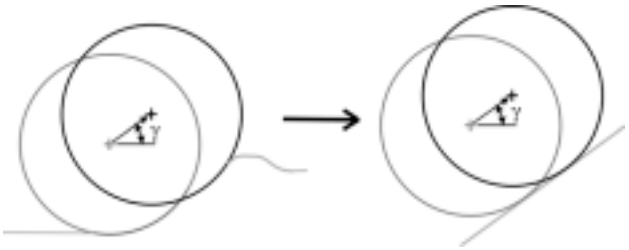

Fig. 5. Wheel–terrain contact angle γ for rigid wheel on deformable terrain.

of travel imposed on the wheel by the terrain during motion (see Figure 5).

In Figure 4, the rear and front wheels make contact with the terrain at angles γ_1 and γ_2 from the horizontal, respectively. The vehicle pitch, α, is also defined with respect to the horizontal. The wheel centers have speeds v_1 and v_2. These speeds are in a direction parallel to the local wheel–terrain tangent due to the rigid terrain assumption. The distance between the wheel centers is defined as l.

For this system, the following kinematic equations can be written:

$$v_1 \cos(\gamma_1 - \alpha) = v_2 \cos(\gamma_2 - \alpha) \tag{13}$$

$$v_2 \sin(\gamma_2 - \alpha) - v_1 \sin(\gamma_1 - \alpha) = l\dot{\alpha}. \tag{14}$$

Equation (13) represents the kinematic constraint that the wheel center length l does not change. Note that this constraint remains valid in cases where l varies, such as articulated suspension vehicles, as long as l is measurable and varies slowly. Equation (14) is a rigid-body kinematic relation between the velocities of the wheel centers and the vehicle pitch rate, $\dot{\alpha}$.

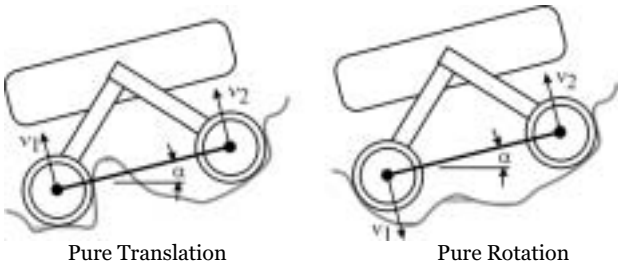

Fig. 6. Physical interpretations of $\cos\theta = 0$.

Combining eqs. (13) and (14) yields

$$\sin(\gamma_2 - \alpha - (\gamma_1 - \alpha)) = \frac{l\,\dot{\alpha}}{v_1}\cos(\gamma_2 - \alpha). \tag{15}$$

With the definitions

$$\theta \equiv \gamma_2 - \alpha,\ \beta \equiv \alpha - \gamma_1, a \equiv {}^{l\,\dot{\alpha}}/_{v_1}, b \equiv {}^{v_2}/_{v_1}$$

Eqs. (13) and (15) become

$$(b\sin\theta + \sin\beta)\cos\theta = a\cos\theta \tag{16}$$

$$\cos\beta = b\cos\theta. \tag{17}$$

Solving eqs. (16) and (17) for the wheel–terrain contact angles γ_1 and γ_2 yields

$$\gamma_1 = \alpha - \cos^{-1}(h) \tag{18}$$

$$\gamma_2 = \cos^{-1}({}^{h}/_{b}) + \alpha \tag{19}$$

where

$$h \equiv \frac{1}{2a}\sqrt{2a^2 + 2b^2 + 2a^2b^2 - a^4 - b^4 - 1}.$$

There are two special cases that must be considered in this analysis. The first special case occurs when the rover is stationary. In this case, eqs. (16) and (17) do not yield a solution, since, if $\dot{\alpha} = v_1 = v_2 = 0$, both a and b are undefined. Physically, the lack of a solution results from the fact that a stationary rover can have an infinite set of possible contact angles at each wheel.

The second special case occurs when $\cos\theta$ equals zero. In this case, $\gamma_2 = \pm\pi/2 + \alpha$ from the definition of θ, and eq. (18) yields the solution $\gamma_1 = \pm\pi/2 + \alpha$. Physically, this corresponds to two possible cases: the rover undergoing pure translation or pure rotation (see Figure 6).

While these cases are unlikely to occur in practice, they are easily detectable. For the case of pure rotation, $v_1 = -v_2$. The solutions for γ_1 and γ_2 can be written by inspection as

$$\gamma_1 = \alpha + \frac{\pi}{2}sgn(\dot{\alpha}) \tag{20}$$

$$\gamma_2 = \alpha - \frac{\pi}{2} sgn\,(\dot{\alpha})\,. \tag{21}$$

For the case of pure translation, $\dot{\alpha} = 0$, and $\nu_1 = \nu_2$. Thus, h is undefined and the system of eqs. (16) and (17) has no solution. However, for low-speed rovers considered in this work, the terrain profile varies slowly with respect to the data sampling rate. It is reasonable to assume that wheel–terrain contact angles computed at a given time-step will be similar to contact angles computed at the previous time-step. Thus, previously estimated contact angles can be used when a solution to the estimation equations does not exist.

The pitch and pitch rate can be measured with inclinometers and rate gyroscopes. The wheel center speeds can be estimated from the wheel angular rate as measured by a tachometer, provided the wheels do not have substantial slip. For rovers equipped with a forward-looking stereo camera pair, wheel center speeds can be computed via techniques such as visual odometry even in the presence of substantial slip (Olson et al. 2000). Thus, wheel–terrain contact angles can be estimated with common, low-cost on-board sensors. The estimation process is computationally simple, and thus suitable for on-board implementation.

4.1. Extended Kalman Filter Implementation

The above analysis suggests that wheel–terrain contact angles can be computed from simple, measurable quantities. However, sensor noise and wheel slip will degrade these measurements. Here, an extended Kalman filter (EKF) is developed to compensate for these effects. This filter is an effective framework for fusing data from multiple noisy sensor measurements to estimate the state of a nonlinear system (Brown and Hwang 1997; Welch and Bishop 1999). In this case, the sensor signals are wheel tachometers, gyroscopes, and inclinometers, and are assumed to be corrupted by unbiased Gaussian white noise with known covariance. Again, due to the assumption of quasi-static vehicle motion, inertial effects do not corrupt the sensor measurements. Also, we assume that sensor bandwidth is significantly faster than the vehicle dynamics, and thus sensor dynamics do not corrupt the sensor measurements.

Here we attempt to estimate the state vector $\mathbf{x}$, composed of the wheel–terrain contact angles, i.e., $\mathbf{x} = \begin{bmatrix} \gamma_1 & \gamma_2 \end{bmatrix}^T$. The discrete-time equation governing the evolution of $\mathbf{x}$ is

$$\mathbf{x}_{k+1} = \begin{bmatrix} 1 & 0 \\ 0 & 1 \end{bmatrix} \mathbf{x}_k + w_k \tag{22}$$

where w_k is a 2×1 vector representing the process noise. Equation (22) implies that ground contact angle evolution is a random process. This is physically reasonable, since terrain variation is inherently unpredictable. The elements of w can be assigned as the expected terrain variation:

$$w_k = \mathrm{E}\,(\mathbf{x}_{k+1} - \mathbf{x}_k)\,. \tag{23}$$

This information can be estimated from knowledge of local terrain roughness, or computed from forward-looking range data.

The EKF measurement equation can be written as

$$\mathbf{y}_k = \begin{bmatrix} 1 & 0 \\ 0 & 1 \end{bmatrix} \mathbf{x}_k + n_k \tag{24}$$

where $\mathbf{y}_k$ is a synthetic "measurement" of the ground contact angles, computed analytically from eqs. (18) and (19) and raw sensor data, i.e., $\mathbf{y}_k = f(\mathbf{z}_k)$, where $\mathbf{z} = \begin{bmatrix} \alpha & \dot{\alpha} & \nu_1 & \nu_2 \end{bmatrix}^T$. We assume that the vehicle pitch α and pitch rate $\dot{\alpha}$ are directly sensed, and speeds ν_1 and ν_2 can be approximated from knowledge of the wheel angular velocities and radii. Noise on the sensory inputs is projected onto the ground contact angle measurements through the noise vector n_k, as $n_k \approx \left[\frac{\partial \mathbf{y}_k}{\partial \mathbf{z}}\right]\Big|_{\mathbf{z}=\mathbf{z}_k} \cdot \begin{bmatrix} \sigma_\alpha & \sigma_{\dot{\alpha}} & \sigma_{\nu_1} & \sigma_{\nu 2} \end{bmatrix}^T$.

The following is a description of the EKF implementation procedure.

1. Initialization of the state estimate $\hat{\mathbf{x}}_0$ and the estimated error covariance matrix $\mathbf{P}_0$. Here, $\hat{\mathbf{x}}_0 = \mathbf{y}_0$, and $\mathbf{P}_0 = \mathbf{R}_x$, where $\mathbf{R}_x = w_0 w_0^T$.

2. Propagation of the current state estimate and covariance matrix. The state estimate is generally computed from a state transition matrix, which here is the identity matrix. Thus

$$\hat{\mathbf{x}}_k^- = \hat{\mathbf{x}}_{k-1}^-. \tag{25}$$

The covariance matrix is computed as

$$\mathbf{P}_k^- = \mathbf{P}_{k-1} + \mathbf{R}_x. \tag{26}$$

3. Computation of the Kalman gain, and updating the state estimate and covariance matrix. The Kalman gain matrix $\mathbf{K}$ is given by

$$\mathbf{K}_k = \mathbf{P}_k^- \left(\mathbf{P}_k^- + \mathbf{R}_{y_k}\right)^{-1}. \tag{27}$$

We can compute the sensor noise matrix $\mathbf{R}_{y_k}$ as

$$\mathbf{R}_{y_k} = n_k n_k^T = \left(\frac{\partial \mathbf{y}_k}{\partial \mathbf{z}}\right)^T \mathbf{R}_z \left(\frac{\partial \mathbf{y}_k}{\partial \mathbf{z}}\right) \tag{28}$$

where $\mathbf{R}_z$ is a 4×4 diagonal matrix of known noise covariances associated with $\mathbf{z}$: $\mathbf{R}_z = diag\left(\sigma_\alpha^2, \sigma_{\dot{\alpha}}^2, \sigma_{\nu_1}^2, \sigma_{\nu_2}^2\right)$. Note that estimates of $\mathbf{R}_{y_k}$ and $\mathbf{y}_k$ can be formed by computing the unscented transform of eqs. (18) and (19) (Julier and Uhlmann 1997).

The state estimate is updated as

$$\hat{\mathbf{x}}_k = \hat{\mathbf{x}}_k^- + \mathbf{K}_k \left(\mathbf{y}_k - \hat{\mathbf{x}}_k^-\right) \tag{29}$$

and the covariance matrix is updated as

$$\mathbf{P}_k = (\mathbf{I} - \mathbf{K}_k)\,\mathbf{P}_k^-. \tag{30}$$

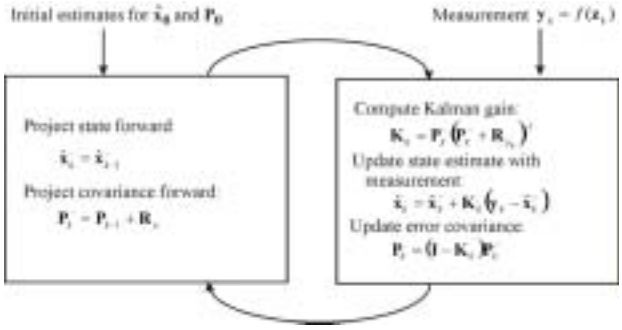

Fig. 7. EKF operation diagram.

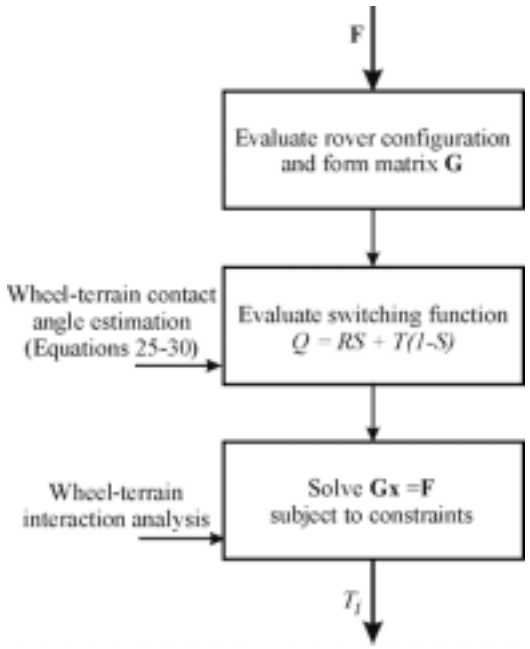

Fig. 8. Block diagram of rough-terrain control algorithm.

The special cases discussed in Section 4 can lead to a lack of observability in the filter. However, as described above, these situations are easily detectable. Thus, new measurement updates for the filter are not taken when these special cases are detected.

See Figure 7 for a pictorial diagram of the EKF estimation process (adapted from Welch and Bishop 1999).

The rough-terrain control algorithm is summarized in Figure 8.

5. Simulation Results

The performance of the multicriteria rough-terrain control algorithm and traditional individual-wheel velocity control were compared in simulation. The simulated system was a planar, two-wheeled 10 kg vehicle similar to that shown in Figure 4. The rigid wheel radius r was 10 cm and its wheel width w was 15 cm. The wheel spacing l was 0.8 m. Measured quantities were vehicle pitch and wheel angular velocities. Sensor noise was modeled by white noise of standard deviation approximately equal to 5% of the full-range values.

The force distribution equations for the simulated system can be written as

$$\begin{bmatrix} \cos(\gamma_1) & -\sin(\gamma_1) & \cos(\gamma_2) & -\sin(\gamma_2) \\ \sin(\gamma_1) & \cos(\gamma_1) & \sin(\gamma_2) & \cos(\gamma_2) \\ V_1^y & -V_1^x & V_2^y & -V_2^x \end{bmatrix} \begin{bmatrix} T_1 \\ N_1 \\ T_2 \\ N_2 \end{bmatrix} = \begin{bmatrix} F_x \\ F_y \\ M_z \end{bmatrix}. \tag{31}$$

This system of equations possesses $(2n - 3) = 1$ degree of redundancy. Thus, there exists a free variable that can be selected based on the dual-criteria optimization method discussed above.

The terrain was modeled as a moderately dense deformable soil similar to that which has been observed on Mars (NASA 1988; Matijevic et al. 1997). The following parameters were used: cohesion $c = 1.0$ kPa; internal friction angle $\phi = 35°$; sinkage coefficient $n = 1$; cohesive modulus of deformation $K_c = 10$ kN/m^{n+1}; frictional modulus of deformation $K_\phi = 850$ kN/m^{n+2}; shear deformation modulus $K = 0.03$ m.

At each simulation time increment, the wheel sinkage, motion resistance, and wheel thrust were computed as a function of the soil parameters and the applied wheel torque.

Wheel sinkage was computed in order to determine the motion resistance due to soil compaction. Sinkage was computed for each wheel i as (Wong 2001)

$$z_i = \left[\frac{3N_i}{b\,(3-n)\left(K_c/b + K_\phi\right)\sqrt{2r}} \right]^{(2/(2n_s+1))}. \tag{32}$$

The motion resistance due to soil compaction was determined by (Wong 2001)

$$R_i = b\left[\left(\frac{K_c}{b} + K_\phi \right) \frac{z_i^{n+1}}{n+1} \right]. \tag{33}$$

The wheel thrust was computed as (Wong 2001)

$$TH = r^2 b \int_0^{\theta_1} \left(c + \left(\left(\frac{k_c}{b} + k_\phi \right) (r\,(\cos\theta - \cos\theta_1))^n \right) \tan\phi \right) \times \left(1 - \exp\left(-\frac{r}{k} \left[\theta_1 - \theta - (1-i)\,(\sin\theta_1 - \sin\theta) \right] \right) \right) \cos(\theta)\, d\theta. \tag{34}$$

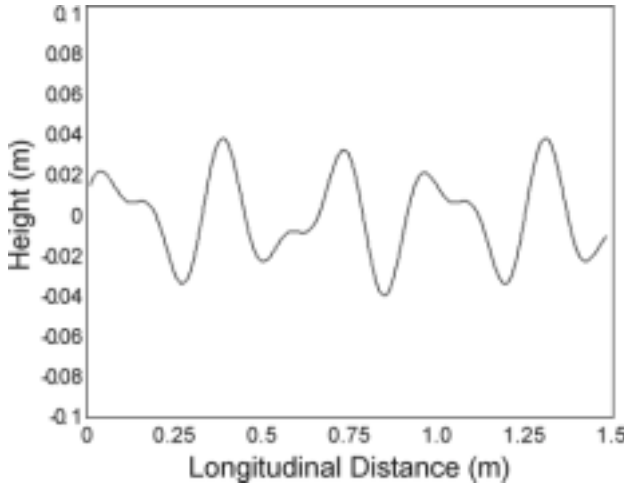

Fig. 9. Simulated benign terrain profile.

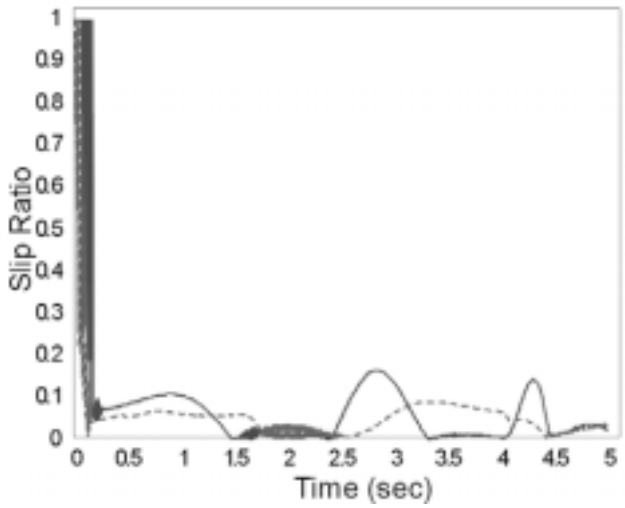

Fig. 10. Average slip ratio of front and rear wheels for rough-terrain control system (dashed) and velocity-controlled system (solid).

Two sets of simulation results are presented below. The first simulation was the traverse of gently rolling terrain, as seen in Figure 9. The velocity-controlled system was commanded by an individual-wheel PID control scheme with a desired angular velocity of 2.5 rad s^{-1}. The rough-terrain control system was commanded by a horizontal inertial force vector of magnitude equal to the difference between the desired body velocity of 25 cm s^{-1} and the actual body velocity, divided by the vehicle mass. The dual-criteria optimization threshold C was set equal to 15°, since terrain with ground-contact angles less than 15° can generally be considered benign.

Both the velocity-controlled system and the rough-terrain control system successfully traversed the benign terrain. However, the energy consumed by the rough-terrain control system was 14.5 J compared to 23.5 J by the velocity-controlled system, an improvement of 38.3%. This power saving is due to reduced wheel slip, as shown in Figure 10. The rough-terrain control system has an average slip ratio of 5.3% during the traverse while the velocity-controlled system has an average slip of 9.4%. The dual-criteria optimization was in energy minimization mode during most of the traverse. Thus, even in relatively gentle terrain the rough-terrain control can be beneficial by reducing power consumption.

Figure 11 shows the performance of the wheel–terrain contact angle estimation algorithm. The estimated terrain contact angles remain very near the actual terrain contact angles for the duration of the simulation.

The second simulation was the traverse of highly challenging terrain, seen in Figure 12. The maximum slopes in this terrain are near the internal friction angle of the soil. Control parameters were the same as the previous simulation.

In this simulation the rough-terrain control system is able to complete the traverse while the velocity-controlled system is not. This is due to the additional thrust force generated by the rough-terrain control algorithm, shown in Figure 13. The total wheel thrust generated by the rough-terrain control system remains higher than the thrust generated by the velocity-controlled system during most of the traverse. In this case, the rough-terrain control system commands increased torque to the rear wheel, which has a much higher load than the front wheel, resulting in increased net thrust. The dual-criteria optimization remained in traction maximization mode for the majority of the traverse.

The average wheel slip in the rough-terrain control system remained lower than the velocity-controlled system during most of the traverse, as seen in Figure 14. Note that although significant slip remained in the rough-terrain control system, this is due to the highly rough terrain.

6. Experimental Results

The rough-terrain control algorithm was applied to a six-wheeled experimental microrover operating in an indoor rough-terrain environment (see Figure 15). First, a go/no-go ditch traversal experiment was performed to examine the mobility improvement provided by the rough-terrain control algorithm compared to individual-wheel velocity control.

The microrover was commanded to traverse a ditch covered by loose, sandy soil. The maximum depth of the ditch was approximately one wheel diameter. The width of the ditch varied from approximately two to four wheel diameters. The wheel–terrain contact angles were observed to vary greatly during traversal of the ditch (see Figure 16). Thus, ditch traversal is a challenging mobility task.

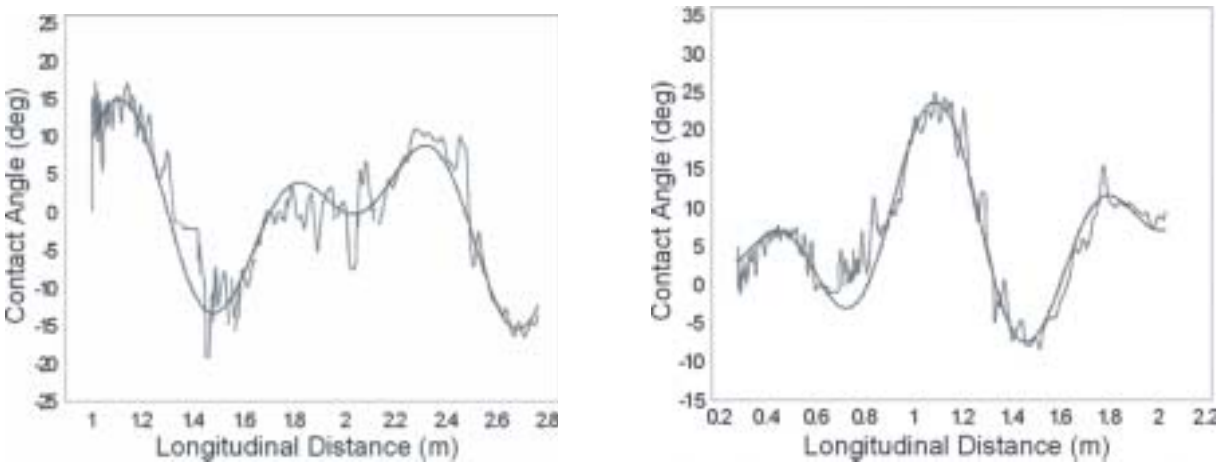

Front Wheel **Rear Wheel**

Fig. 11. Wheel–terrain contact angle estimation of front and rear wheels during benign terrain traverse.

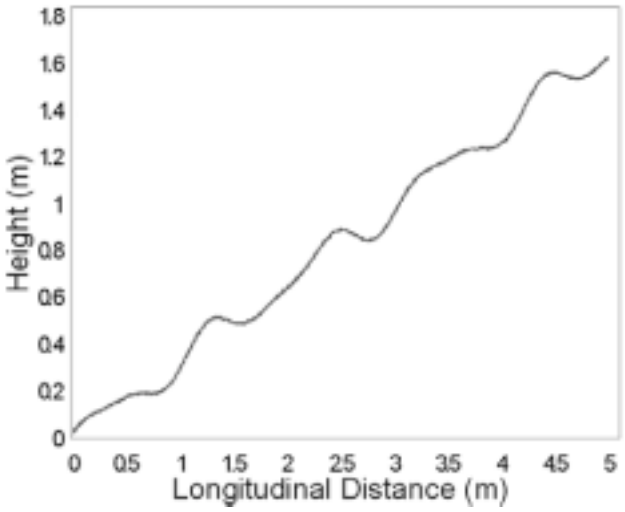

Fig. 12. Simulated challenging terrain.

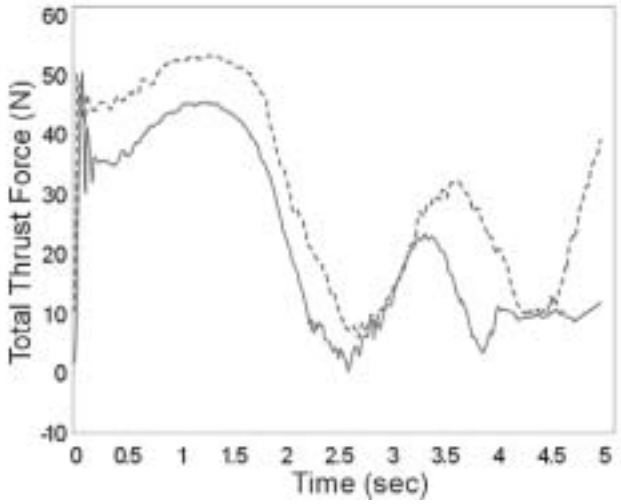

Fig. 13. Total wheel thrust of rough-terrain control system (dashed) versus velocity-controlled system (solid).

It was observed that the velocity-controlled system successfully completed the traverse six times out of 20, while the rough-terrain control system successfully traversed the ditch 14 times out of 20, an improvement of 133%. Variability in the results is due to irregularity in soil compactness and distribution, ditch traversal route, and commanded velocity (in the velocity-controlled system) and body force vector (in the rough-terrain control system).

Mobility improvement due to rough-terrain control can be understood by examining a time history of the rover's right-side wheel normal forces during ditch traversal, shown in Figure 17. At time $t = 0$, when the rover is on flat terrain, it can be seen that the system weight is unevenly distributed, with the rear wheel bearing approximately 49% of the rover weight, the middle wheel bearing 35%, and the front wheel 16%. This is due to the kinematic configuration of the rocker-bogie suspension. During traversal, the normal forces vary as much as 87% compared to their initial values.

The velocity controller applies the torque necessary to achieve a desired angular velocity. This results in applied thrust that is generally either less than or greater than the maximum thrust the soil can bear. If the applied thrust is less

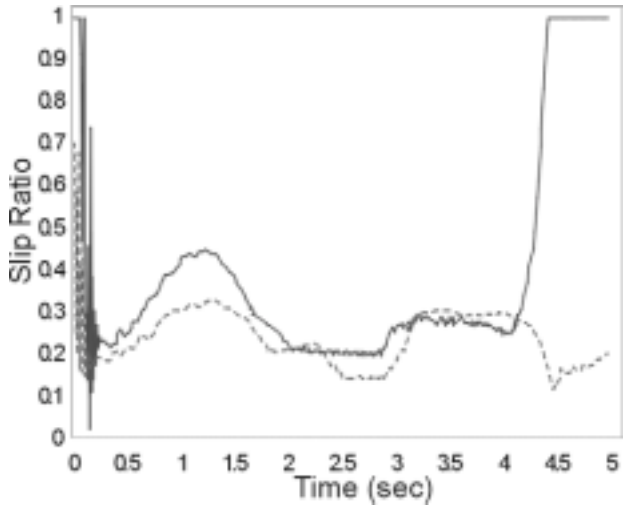

Fig. 14. Average slip ratio of front and rear wheels of rough-terrain control system (dashed) versus velocity-controlled system (solid).

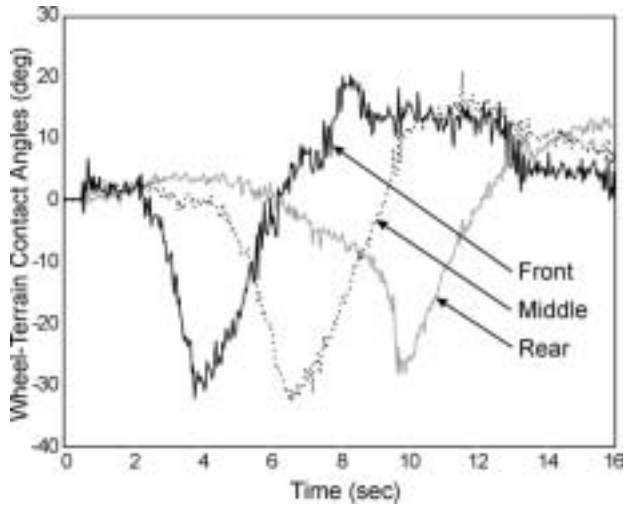

Fig. 16. Wheel–terrain contact angles during ditch traversal (right side contact angles shown).

Fig. 15. Experimental microrover during go/no-go ditch traversal experiment.

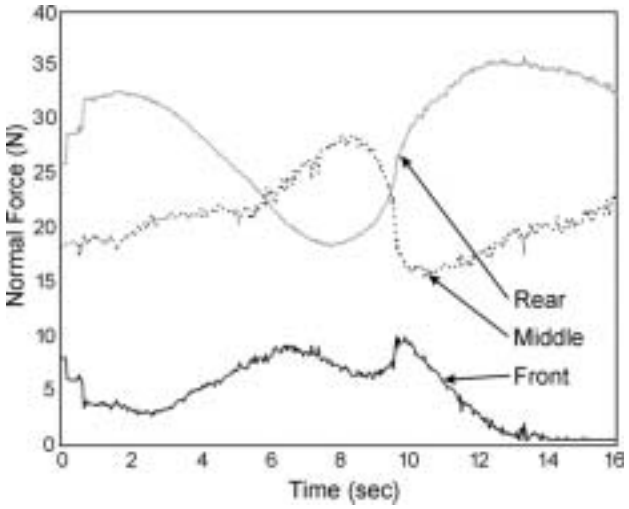

Fig. 17. Normal forces during ditch traversal (right side forces shown).

than maximum, the resulting total thrust exerted by the rover is suboptimal. If the applied thrust is greater than maximum, soil failure occurs, and wheel slip results.

Conversely, the rough-terrain control system attempts to apply the maximum thrust the soil can bear. Thus, the rear wheel (which has high normal force) is commanded greater torque than the front wheel (which has a low normal force). The resulting net vehicle thrust is greater than the velocity-controlled system, resulting in improved rough-terrain mobility.

In these experiments, estimates of the terrain parameters c and ϕ were based on results obtained from parameter identification experiments. Results of a representative experiment are shown in Figure 18.

A second experiment was performed to quantify the thrust increase generated by the rough-terrain control algorithm. A weighted aluminum sled was attached to a force/torque sensor

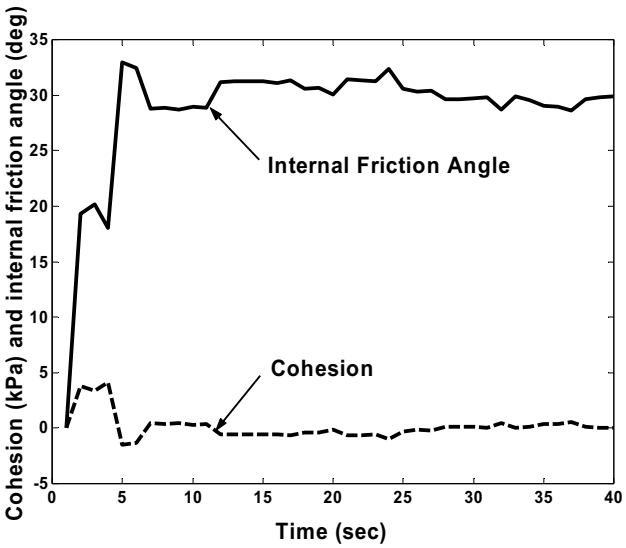

Fig. 18. Estimation results for cohesion and internal friction angle of sand.

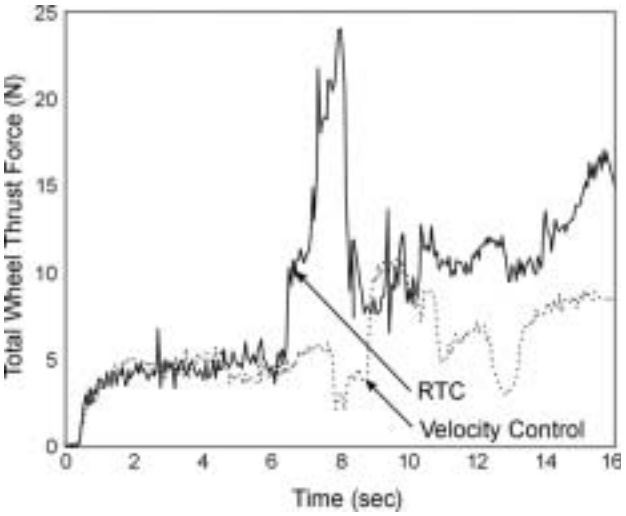

Fig. 20. Thrust force during ditch traversal with rough-terrain control (solid) and velocity control (dotted).

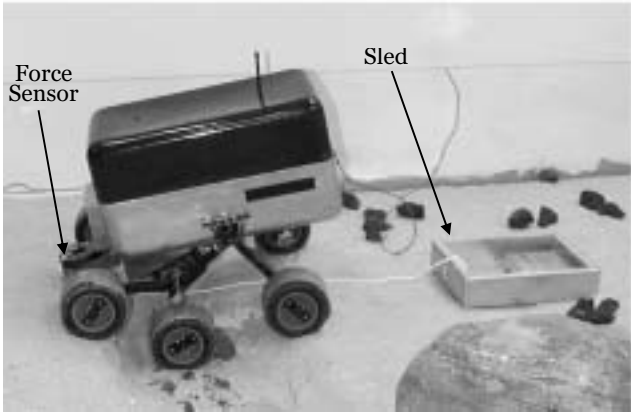

Fig. 19. Microrover during thrust force measurement experiment.

mounted at the front of the rover, as shown in Figure 19. The force exerted on the sled was measured during the ditch traverse with a six-axis force/torque sensor.

Results of a representative pair of trials are shown in Figure 20. It can be seen that the rough-terrain control system generated greater thrust than the velocity-controlled system during the majority of the traverse. Again, this thrust increase is due to optimization of the wheel-torque distribution by the rough-terrain control algorithm. The average thrust improvement was 82%, a substantial improvement. This thrust improvement allows a rough-terrain control rover to traverse more challenging terrain than a velocity-controlled rover.

7. Conclusions

In this paper a rough-terrain control method has been presented that optimizes force distribution for improved traction or reduced power consumption, depending on the local terrain profile. A wheel–terrain contact angle estimation algorithm has also been presented, along with a brief discussion of a terrain parameter estimation method. The algorithm is based on rigid-body kinematic equations and utilizes an EKF to fuse noisy sensor signals. Simulation results for a planar model of a four-wheeled rover have shown that the control algorithm consumes less power and provides greater mobility than traditional individual-wheel velocity control. Experimental results on a six-wheeled microrover have shown that the rough-terrain control method results in measurably improved mobility over challenging terrain.

Acknowledgments

This work was supported by the NASA JPL. The authors would like to acknowledge the support of Drs Paul Schenker, Samaad Hayati, and Richard Volpe at JPL.

References

Balaram, J. 2000. Kinematic state estimation for a Mars rover. *Robotica* 18:251–262.

Bekker, G. 1956. *Theory of Land Locomotion*, University of Michigan, Ann Arbor.

Bekker, G. 1969. *Introduction to Terrain-Vehicle Systems*, University of Michigan Press, MI.

Brown, R. and Hwang, P. 1997. *Introduction to Random Signals and Applied Kalman Filtering,* Wiley, New York.

Chung, W. and Waldron, K. 1993. Force distribution by optimizing angles for multifinger systems. *Proceedings of the IEEE International Conference on Robotics and Automation (ICRA)*, Atlanta, GA, Vol. 3, pp. 717–722.

Cunningham, J., Roberts, J., Corke, P., and Durrant-Whyte, H. 1998. Automation of underground LHD and truck haulage. *Proceedings of Australian IMM Annual Conference*, pp. 241–246.

Dubowsky, S., Moore, C., and Sunada, C. 1995. On the design and task planning of power-efficient field robotic systems. *Proceedings of the 6th ANS Robotics and Remote Systems Conference.*

Farritor, S., Hacot, H., and Dubowsky, S. 1998. Physics-based planning for planetary exploration. *Proceedings of the IEEE International Conference on Robotics and Automation (ICRA)*, Leuven, Belgium, pp. 278–283.

Golombek, M.P. 1998. Mars Pathfinder mission and science results. *Proceedings of the 29th Lunar and Planetary Science Conference.*

Gonthier, Y. and Papadopoulos, E. 1998. On the development of a real-time simulator for an electro-hydraulic forestry machine. *Proceedings of the IEEE International Conference on Robotics and Automation (ICRA)*, Leuven, Belgium.

Hacot, H. 1998. *Analysis and Traction Control of a Rocker-Bogie Planetary Rover.* MS Thesis, Massachusetts Institute of Technology, Cambridge, MA.

Hung, M., Orin., D., and Waldron, K. 1999. Force distribution equations for general tree-structured robotic mechanisms with a mobile base. *Proceedings of the IEEE International Conference on Robotics and Automation (ICRA)*, Detroit, MI, pp. 2711–2716.

Iagnemma, K., Shibly, H., and Dubowsky, S. 2002. On-line terrain parameter estimation for planetary rovers. *Proceedings of the IEEE International Conference on Robotics and Automation (ICRA*), Washington, DC, May 11–15.

Iagnemma, K., Kang, S., Brooks, C., and Dubowsky, S. 2003. Multi-sensor terrain estimation for planetary rovers. *Proceedings of the 7th International Symposium on Artificial Intelligence, Robotics and Automation in Space (i-SAIRAS).*

Julier, S., and Uhlmann, J. 1997. A new extension of the Kalman filter to nonlinear systems. *Proceedings of the International Symposium of Aerospace/Defense Sensing, Simulation and Controls.*

Kawabe, T., Nakazawa, M., Notsu, I., and Watanabe, Y. 1997. Sliding mode controller for wheel slip ratio control system. *Vehicle System Dynamics* 27(5–6):393–408.

Kumar, V. and Waldron, K. 1988. Force distribution in closed kinematic chains. *IEEE Transactions on Robotics and Automation* 4(6):657–644.

Kumar, V. and Waldron, K. 1990. Force distribution in walking vehicles. *ASME Journal of Mechanical Design* 112:90–99.

Lee, H. and Tomizuka, M. 1996. Adaptive vehicle traction force control for intelligent vehicle highway systems. *Proceedings of the ASME Conference on Dynamics, Systems, and Control,* pp. 17–24.

Matijevic, J. et al. (Rover Team). 1997. Characterization of the Martian surface deposits by the Mars Pathfinder Rover, Sojourner. *Science* 278:1765–1768.

Mishkin, A., Morrison, J., Nguyen, T., Stone, H., Cooper, B., and Wilcox, B. 1998. Experiences with operations and autonomy of the Mars Pathfinder Microrover. *Proceedings of the 1998 IEEE Aerospace Conference*, pp. 337–51.

NASA. 1988. Environment of Mars. NASA Technical Memorandum 100470, Lyndon B. Johnson Space Center.

Olson, C., Matthies, L., Schoppers, M., and Maimone, M. 2000. Robust stereo ego-motion for long distance navigation. *Proceedings of the IEEE Conference on Computer Vision and Pattern Recognition*, Vol. 2, pp. 453–458.

Osborn, J. 1989. Applications of robotics in hazardous waste management. *Proceedings of the SME 1989 World Conference on Robotics Research.*

Reister, D. and Unseren, M. 1993. Position and constraint force control of a vehicle with two or more steerable drive wheels. *IEEE Transactions on Robotics and Automation* 9:723–731.

Schenker, P., Huntsberger, T., Pirjanian, P., Baumgartner, E., and Tunstel, E. 2003. Planetary rover developments supporting Mars exploration, sample return and future human-robotic colonization. *Autonomous Robots* 14:103–126.

Sreenivasan, S. and Waldron, K. 1996. Displacement analysis of an actively articulated wheeled vehicle configuration with extensions to motion planning on uneven terrain. *Transactions of the ASME Journal of Mechanical Design* 118:312–317.

Sreenivasan, S. and Wilcox, B. 1994. Stability and traction control of an actively actuated microrover. *Journal of Robotic Systems* 11(6):487–502.

Tan, H. and Chin, Y. 1992. Vehicle antilock braking and traction control: a theoretical study. *International Journal of Systems Science* 23(3):351–365.

Volpe, R. 2003. Rover functional autonomy development for the Mars Mobile Science Laboratory. *Proceedings of 2003 IEEE Aerospace Conference.*

Welch, G., and Bishop, G. 1999. *An Introduction to the Kalman filter.* Technical report TR 95-041, Department of Computer Science, University of North Carolina, Chapel Hill.

Wong, J. 2001. *Theory of Ground Vehicles,* 3rd edition, Wiley Interscience, New York.